Efficient conversion of ethanol to acetaldehyde with induction heating at low temperature

Han Wang [a], Ben Ko [a], John O'Donnell-Sloan [b], John Minh Quang Pham [a], Hannah Schutte [c], Nicholas Wang [a], Carlos Lizandara-Pueyo [d], Jian-Ping Chen [e], Erdem Sasmaz [a,*]

[a] Department of Chemical and Biomolecular Engineering, University of California, Irvine, CA 92697, USA
[b] Department of Chemical and Biological Engineering, Northwestern University, Evanston, IL 60208, USA
[c] Department of Chemical Engineering, Carnegie Mellon University, Pittsburgh, PA 15213, USA
[d] BASF SE, Carl-Bosch Strasse 38, 67056 Ludwigshafen am Rhein, Germany
[e] BASF Corporation, 23800 Mercantile Road, Beachwood, OH 44122, USA

ARTICLE INFO

ABSTRACT

The application of induction heating (IH) to provide heat for chemical reactions has received great attention due to its potential to electrify chemical reactions. Biomass-based production of acetaldehyde from ethanol has gained rising interest since it provides an alternative sustainable method instead of the fossil-fuel-based output using acetylene and formaldehyde in the presence of a catalyst. The dehydrogenation of ethanol can be catalyzed by supported copper catalysts. The reaction is typically carried out at high temperatures, around 250–300 °C, without oxygen. The resulting product mixture usually contains acetaldehyde, as well as other byproducts such as ethylene and hydrogen gas. The acetaldehyde can be separated from the other components using distillation or other separation techniques. In this work, we studied the catalyst activity with IH for the first time and achieved high ethanol conversion and acetaldehyde selectivity at a temperature of 30 °C lower than that with conventional furnace heating (CFH). A transport model was applied to design the catalyst bed configuration and improve the catalyst activity, stability, and energy efficiency by minimizing the temperature gradient. Our work suggests that the temperature distribution and the fast compensation of heat loss through IH are critical for the catalyst behavior. Both high production efficiency and energy efficiency can be achieved with IH, such that it can be an efficient and environment-friendly heating method for the chemical industry.

1. Introduction

With the increasing global demand for chemical products, there is a pressing need to prioritize the development and implementation of sustainable chemical production methods. It is crucial to reassess the ongoing investment in emission-intensive production technologies. Chemical manufacturing predominantly relies on fossil fuels as an energy source to provide heat for the reactions, which is one source of greenhouse gas emissions [1]. The urgency to use low-carbon emitting technologies in the chemical industry has led to a push towards utilizing renewable electricity as the primary source for process energy, replacing traditional fossil fuels [1]. This situation has led to the electrification of chemical reactions using electrochemical processes or electrification of heating processes. The latter involves replacing traditional fossil-fuel-based heating methods with electric heating technologies such as

resistive heating [2], induction heating (IH), or microwave heating [3]. Among them, IH can provide localized heating generated on ferromagnetic materials which can act as an active site and heating element [4,5].

Although being explored in various applications, from cancer treatment in the medical field to metallurgic manufacturing on an industrial scale, IH has not been studied in the catalysis field until recently [1]. In IH, an alternating electromagnetic field interacts with unpaired electron spins of ferromagnetic materials, generating a strong magnetic energy [6]. The absorbed magnetic energy is released as heat due to the hysteresis losses. This mechanism allows direct heating of the materials, allowing the catalysts to be operated under a kinetically controlled regime [7,8]. When compared to conventional furnace heating (CFH), IH heating offers several advantages: (1) instantaneous on/off switching of the heat supplied to the catalytic bed [4,8], (2) elimination of hot spots in exothermic reactions [9], (3) reduced heat transfer limitation

---

[10–12], (4) enhanced reaction kinetics and decreased occurrence of side reactions, and uniform reaction temperatures can lead to enhanced catalytic activity [13–22], (5) less energy consumption than the conventional heating reactors with heat losses (up to 90 % energy efficiency) [11], and (6) direct use of renewable sources such as wind, solar, and hydropower for energy production [5,23]. IH directly targets the susceptors inside the reactor instead of heating the catalyst bed through conduction and convection from the external heating source so that the desired temperature can be reached within an extremely short time. This helps to reduce energy consumption since it has the highest power transmission, overcome the heating inertia, and reduce energy waste [10].

The first IH application in catalysis was proposed by Ceylan *et al.*, pointing out the possibility of utilizing Co, Ni, Fe_3O_4/Fe_2O_3, and their alloys as efficient heating materials for chemical synthesis [24]. While many metals and metal oxides show magnetism under the magnetic field (MF), ferromagnetic materials such as Co, Ni, and Fe are primarily selected in the reactions to provide the heating through hysteresis loss. The Curie temperatures (Tc) of Co, Ni, and Fe are 1130 ℃, 354 ℃, and 770 ℃, respectively [8,25,26]. The temperature of these metals should not exceed Tc, above which the ferromagnetic materials will become paramagnetic, so the temperature increase with an increasing MF is negligible. In the same year, Liu *et al.* studied the transesterification of canola oil and methanol for biodiesel production using IH with short heating time, showing higher energy efficiency and higher conversion due to the direct interaction between the MF and dipoles and ion pairs in the reactants, which not only provides the heat but also drive further reactions [27].

When IH is applied to catalysis, two types of catalyst beds are used to reach the desired reaction temperature: a physically mixed catalyst bed with a susceptor and the direct use of a magnetically active catalyst [8]. Among these studies, the benefits of applying IH have mainly focused on two aspects: (1) the higher energy efficiency and (2) the higher conversion of the reactants. Lupu, Biris *et al.* concluded that the energy consumption by IH is significantly reduced compared with CFH due to the shortened reaction time when a proper susceptor is selected [28,29]. However, the high energy efficiency of IH is mainly conceptual and a qualitative statement given the fact that only the targeted materials will be heated without the energy loss from convection, conduction, and radiation, which are very common with the CFH [30]. There is a lack of a direct study of the energy consumption of IH.

In our work, we apply IH to the ethanol-to-acetaldehyde (ETAA) reaction for the first time. We have selected the ETAA reaction for several reasons. Firstly, ethanol is a sustainable resource from biomass fermentation. Secondly, the non-oxidative dehydrogenation of ETAA results in the formation of hydrogen and acetaldehyde, a crucial intermediate for the production of resins, solvents, and fragrances, as well as other chemicals, such as acetic acid, ethyl acetate, or n-butanol [31–33]. Supported Cu catalysts have been reported to show excellent ethanol conversion and selectivity to acetaldehyde below 275 ℃ [34]. Finally, the ethanol dehydrogenation reaction is an endothermic process. When using traditional heating methods, uneven temperature distribution within the catalyst bed is expected. This uneven distribution can lead to reduced acetaldehyde selectivity, the formation of undesired side products, and a decrease in the lifetime of the Cu catalyst due to coking and/or metal sintering [35]. However, with the application of IH, these challenges can be overcome. Here, we have physically mixed Co powder as the susceptor in the catalyst bed to provide heating directly to the catalyst. Co was chosen in this work due to its high Curie temperature and large coercivity; thus, it can be more efficient in generating heat through hysteresis losses [36]. A transport model is applied to simulate the temperature distribution and design the configuration of the catalyst bed to improve the catalyst's activity with IH.

2. Methodology

2.1. Materials

BASF Cu 0582E is provided by BASF corporation and contains 52 % CuO on Al_2O_3. Details about the catalyst can be found on Patent US20220152596A1 by Chen et al. [37]. The susceptor Cobalt powder (2 μm particle size, 99.8 % trace metals basis) was purchased from Sigma-Aldrich.

2.2. Characterization

Thermogravimetric analysis (TGA) was conducted with Netzsch TG 209 F1 Libra with a heating rate of 20 ℃/min up to 1100 ℃ under 30 % O_2 in N_2. X-ray Diffraction (XRD) measurements were performed on Rigaku Ultima III equipped with Cu Kα X-ray generator working at 30 kV and 40 mA. The samples were measured from 20° to 90° with the step size of 2°/min at λ = 1.5405 Å.

2.3. Catalyst activity testing

The sketch of the IH reaction system is shown in Fig. S1. The IH heating system (Ambrell EASYHEAT 0224) was equipped with a water-to-air heat exchanger (FLOWMAX-115) to cool down the copper coil during the heating. The coil was customized to ensure the desired frequency and power supply to heat nanomaterials. The 16-turn spiral coil is 6″ long with an I.D. of 5/8″. The frequency stays around 226 kHz during the heating process. A laser pyrometer (Micro-Epsilon, focus: 0.5 mm @ 150 mm) and a PID controller (Omega) were connected to the IH heating system to monitor the reaction temperature. Before the reaction, the pyrometer must be calibrated with a thermocouple to ensure the accuracy of the temperature measurement (Section S1). Co heating layers and the packed catalyst bed containing physically mixed Co powder and Cu/Al_2O_3 catalyst were placed in a fused quartz reactor of 7 mm I.D. x 9.5 mm O.D. with ceramic fiber insulation. The insulated quartz tube was housed inside the induction coil, and the susceptor Co was heated inductively in the applied alternating magnetic field. Detailed dimensions and the susceptor's location and amount are described in Section 2.4.1.

The Cu/Al_2O_3 catalyst was reduced using a 20 % H_2 in N_2 at a total flow rate of 25 ccm for 3 h at 180 ℃. A detailed description of the procedure can be found in the Patent US20220152596A1 by Chen et al. [37]. After reduction, the temperature was subsequently increased to the reaction temperature for the activity tests. Pure ethanol was fed through a liquid pump (New Era NE-4000) and vaporized in an evaporator at 180 ℃. N_2 was used as the carrier gas to provide 5 % ethanol at different weight hourly space velocities (WHSV).

The catalyst activity was also tested with CFH using a clam-shell ceramic fiber furnace (Watlow) to compare with IH. The reaction conditions were the same as those with IH, except no Co heating layers were needed with furnace heating. A K-type thermocouple was inserted inside the reactor to monitor the catalyst bed temperature, while another K-type thermocouple was placed in the furnace to control the reaction temperature through the connection with a PID controller.

The effluent gas from the reactor was analyzed by an SRI gas chromatography (GC) equipped with a flame ionization detector (FID), a methanizer, and a thermal conductivity detector (TCD). The columns used were Hayesep D columns and a Moleseive 5A column. The ethanol conversion (X_{EtOH}), product selectivity (S_i, i = acetaldehyde, methanol, acetic acid, ethyl acetate, acetone), and product yield (Y_i) were calculated as follows:

$$X_{EtOH}(\%) = \frac{C_{EtOH,in} - C_{EtOH,out}}{C_{EtOH,in}} \times 100 \tag{1}$$

$$S_i(\%) = \frac{C_{i,out}}{\sum_{i=1}^{n} C_{i,out}} \times 100 \tag{2}$$

$$Y_i(\%) = X_{EtOH} \times S_i \tag{3}$$

where C_{in} and C_{out} denote the concentration of the component from the inlet and the outlet, respectively. n is the number of the products. The experimental measurement error from the concentration reading is within +/- 5 %.

2.4. Modeling

2.4.1. Geometry

COMSOL Multiphysics simulation was used to construct the reactor geometry in the IH system and analyze the temperature distribution, reaction heat, external heat loss, and fluid dynamics inside the reactor. As shown in Fig. S3, the reactor tube (7 mm ID) in the IH system was modeled axisymmetrically, with a height of 175 mm, and 16 turns of copper coil (3.25 mm ID x 3.75 mm OD). Cooling water through the inner diameter of the coil was modeled to account for additional heat transfer as set up in the IH apparatus. The thickness of the reactor wall (1.25 mm thickness) and ceramic fiber insulation (1.95 mm) layers were constructed in the model to account for the resistance in radial heat transfer. The height of the catalyst bed mixture, cobalt powder, and quartz wool inside the reactor tube was set as 6.11 mm, 0.85 mm, and 15 mm, respectively, measured from the experiment setup.

2.4.2. Governing equations

2.4.2.1. Heat transfer. The electromagnetic heating, heat loss due to the endothermic reaction and external heat loss were considered in the model. The governing field equation for the temperature profile throughout the reactor body was modeled using the conservation of energy as follows:

$$\rho C_p \frac{\partial T}{\partial t} + \rho C_p \vec{u} \cdot \nabla T + \nabla \cdot \vec{q} = Q \tag{4}$$

where T is the temperature, t is time, ρ is the material density, u is the velocity field, C_p and k are the specific heat capacity and thermal conductivity, respectively, determined by the material properties, including air, Co powder, Cu/Al_2O_3 catalyst bed mixed with Co, quartz wool, quartz glass, and ceramic fiber. Finally, q and Q are the heat power vector field and the sum of the endothermic heat consumption described as:

$$\vec{q} = \vec{q}_{cond} + \vec{q}_{conv} + \vec{q}_r \tag{5}$$

$$Q = Q_e + Q_{rxn} \tag{6}$$

where Q_e is the hysteresis loss heat generation of Co powder, and Q_{rxn} is the endothermic heat consumption.

For conduction, Fourier's law was modeled as:

$$\vec{q}_{cond} = -\vec{n}k\nabla T \tag{7}$$

For convection, Newton's law of cooling was modeled as:

$$\vec{q}_{conv} = \vec{n}h(T - T_{amb}) \tag{8}$$

where h is the convection heat transfer coefficient obtained from Churchill and Chu's correlation for external natural convection in the ambient air and internal forced convection with the gas flow [38], and T_{amb} is the surrounding ambient temperature. For radiation heat transfer, Stefan Boltzmann's law was modeled as:

$$\vec{q}_r = \vec{n}\varepsilon\sigma(T^4 - T_{amb}^4) \tag{9}$$

where ε is the surface emissivity and σ is the Stefan-Boltzmann constant. The heat generation from the hysteresis loss, Q_e, is given by the following:

$$Q_e = \omega \oint_{H_{max}} \sigma(H, T)dH \tag{10}$$

The susceptor, metallic Co powder, was the only heating source inside the magnetic field. The heat power from the hysteresis loss of the ferromagnetic cobalt susceptor was determined utilizing the magnetic hysteresis loop obtained from Seong et al. [39]. For computational simplicity, the effective B-H curve was inputted into COMSOL by normalizing the average magnetic flux density in the hysteresis loop to the enclosed area of the loop. Assuming symmetry of the B-H curve allowed only half of the effective B-H curve to be inputted, which yields the hysteresis heat power loss in the COMSOL model, i.e.,

$$Q_e = \frac{1}{2}\sigma_{sm} \cdot H \cdot \omega \cdot \rho_{Co} \tag{11}$$

where σ_{sm} is the specific magnetization of Co powder $[A \cdot m^2 \cdot kg^{-1}]$, taking the applied magnetic field strength as input. ω is the alternating current frequency in the coil, and H is the applied magnetic field. Since the susceptor, Co, is physically mixed with Cu/Al_2O_3 catalyst, the bulk density of Co is calculated by:

$$\rho_{Co} = \frac{m_{Co}}{V_{cat}} \tag{12}$$

$$V_{cat} = \frac{\pi}{4}d^2 h \cdot x_{cat} \tag{13}$$

where m_{Co} is the mass of cobalt powder in the catalyst bed mixture, and V_{cat} is the volume of the catalyst bed in the reactor. d is the inner diameter of the reactor, h is the height of the catalyst bed, x_{cat} is the volume fraction of the Cu/Al_2O_3 catalyst in the catalyst bed.

The heat loss from the reaction Q_{rxn} is determined by:

$$Q_{rxn} = \frac{-\Delta H_{rxn} \cdot \dot{n}_{EtOH} \cdot Y}{V_{cat}} \tag{14}$$

where ΔH_{rxn} is the standard enthalpy change of reaction for ethanol to acetaldehyde, $\dot{n}_{EtOH}$ is the molar feed rate of ethanol at 180 ℃, Y is the yield of acetaldehyde obtained from the reaction at 215 ℃.

Assuming the ideal gas law, the molar flow rate of ethanol, $\dot{n}_{EtOH}$, flowing through the catalyst bed is calculated by:

$$\dot{n}_{EtOH} = \frac{P\dot{V}}{RT_0} \times 0.05 \tag{15}$$

where P is the atmospheric pressure, $\dot{V}$ is the bulk flow rate of the feed gas, R is the ideal gas constant, and T_0 is the gas temperature at standard conditions. 0.05 was multiplied due to the inlet ethanol was 5 % in N_2.

The external heat loss through the inlet and outlet boundaries are calculated by

$$Q_{gas} = \rho_i C_{p,i} \dot{V}(T_i - T) \tag{16}$$

where the subscripted i = in or out, denoting the gas properties of density (ρ), heat capacity (C_p), and temperature at the inlet (T_{in}) and outlet (T_{out}) boundaries of the catalyst bed, respectively.

2.4.2.2. Fluid flow. To account for the heat convection inside the tubular reactor, the momentum conservation of Darcy-Brinkman equations was utilized to model the fluid dynamics of the gas flow. Assuming the absence of internal mass generation, lack of volumetric drag force, and constant porosity, the momentum conservation equations for frequency-transient analysis are:

$$\frac{1}{\epsilon_p}\rho\frac{\partial \vec{u}}{\partial t} = \nabla \cdot \left[-p\vec{I} + \mu\frac{1}{\epsilon_p}\left(\nabla \vec{u}\right.\right.$$
$$\left.\left. + (\nabla \vec{u})^T\right) - \frac{2}{3}\mu\frac{1}{\epsilon_p}(\nabla \cdot \vec{u})\vec{I} \right] - (\mu\kappa^{-1})\vec{u} + \rho\vec{g} \tag{17}$$

$$\nabla \cdot \vec{u} = 0 \tag{18}$$

where ϵ_p is the porosity of the materials in the reactor. The porosities of Co heating layers, the catalyst bed of Co and Cu/Al$_2$O$_3$ mixture, and the quartz wool were measured in the lab, μ is the dynamic viscosity, I is the identity vector, g is the gravitational acceleration constant, T is the transpose operator, and κ is the permeability of the porous medium. No-slip boundary and zero-velocity gradient at the symmetry axis were specified as boundary conditions in the radial direction. The superficial velocity of the reactant feed at the inlet and atmospheric pressure at the outlet boundary were specified for the axial boundary conditions. Fig. S4 (a) shows a uniform velocity profile of the gas flowing through the porous beds in the reactor, implying a steady-state system. Fig. S4 (b) displays a velocity gradient along the radial direction due to the fluid shear stress from the wall, representing the effect of the no-slip boundary condition.

3. Results and discussion

3.1. Catalyst activity enhancement with IH

Before studying the ethanol dehydrogenation with IH, the Co activity was investigated by conducting the reaction under the reaction condition with the CFH, and its effect was confirmed to be minimal, resulting in a 3 % conversion of ethanol (Fig. S5). The catalyst activity of Cu/Al$_2$O$_3$ for ethanol dehydrogenation was then evaluated with IH at different temperatures, using a WHSV of 1.2 h^{-1}. The reaction was also performed with the CFH to establish a baseline, as shown in Fig. 1. As depicted from the time-on-stream (TOS) data in Fig. 1, the ethanol conversion, acetaldehyde selectivity, and acetaldehyde yield were compared at temperatures of 215 ℃, 225 ℃, 235 ℃, and 245 ℃ with both IH and CFH. The ethanol conversion with the CFH was 54.1 % and 57.9 % at 215 ℃ and 225 ℃, respectively. When Co powder was mixed with the catalyst, CFH showed similar results to the catalyst bed with IH (Fig. S6), suggesting minimal impact of Co powder on catalyst activity. However, the ethanol conversion significantly improved with IH, reaching 82.5 % and 80.8 % at 215 ℃ and 225 ℃, respectively, achieving the equilibrium conversion of ethanol dehydrogenation reaction. The deactivation with IH can be observed with time, which will be discussed in Section 3.2. A similar deactivation trend was reported by Liu *et al.* for the non-oxidative ethanol dehydrogenation to acetaldehyde reaction over Au/MgCuCr$_2$O$_4$ catalyst [40]. The selectivity to acetaldehyde was not affected by the different heating methods, indicating the increase in conversion was most likely due to the enhanced heat transfer through the close contact between Co and Cu/Al$_2$O$_3$ particles and improved local temperature distribution rather than changes in the reaction mechanisms.

In order to assess the impact of IH on the enhancement of catalytic activity, the reaction temperature was increased to 245 ℃ and above with the CFH (Fig. 1). It was observed that ethanol conversion and

acetaldehyde selectivity under CFH matched those achieved with the IH when the temperature was increased by 30 ℃ within the first 15 h at 245 ℃ and 255 ℃. This notable improvement in the ethanol conversion at lower temperatures has also been reported in other reactions, such as the hydrogenation of fatty acid, steam reforming of methane, and Fisher-Tropsch synthesis [4,30,41]. The convergence of ethanol conversion and product selectivities between IH and CFH at elevated reaction temperatures indicates that IH has the potential to enhance energy efficiency and production efficiency by reducing the reaction temperature by 30 ℃. As the susceptor (Co powder) is thoroughly mixed with Cu/Al$_2$O$_3$ in the catalyst bed, rapid heat compensation between particles can be provided directly and immediately to the catalyst through close contact during the endothermic reaction. For CFH, the heat supply depends on heat transfer through the gas phase and reactor wall, which can result in temperature fluctuations and gradients. This slow response to local heat loss caused by the reaction can consequently limit the catalyst activity.

The catalyst activity was investigated at different WHSVs using both IH and CFH. The ethanol conversion, and acetaldehyde selectivity and yield were tested for 15 h at WHSVs of 0.6 h^{-1} and 1.2 h^{-1}. As shown in Fig. 2 (a-c), the WHSV significantly impacted the conversion, selectivity, and yield. Such differences can be attributed to the changes in the contact time between ethanol vapor and the catalyst surface. A lower WHSV of 0.6 h^{-1} increased the contact time, leading to a secondary reaction where more ethyl acetate was formed through the acetaldehyde coupling with ethanol and followed by further dehydrogenation (Fig. S7 (a)) [42,43]. Consequently, a higher ethanol conversion of over 80 % was achieved within the first 5 h, and a lower acetaldehyde selectivity of 30 % to 68 % was observed through the 15 h reaction time. The longer contact time also contributed to the acetone formation due to the significant amount of adsorbed acetaldehyde undergoing a condensation reaction (Fig. S7 (b)). The catalyst activity at WHSV of 0.6 h^{-1} and 1.2 h^{-1} was studied with CFH, as shown in Fig. 3 and Fig. S8. The average ethanol conversion was 47 % and 58 % at 1.2 h^{-1} and 0.6 h^{-1}, respectively. The selectivity of acetaldehyde decreased to 48 % – 69 % over the reaction time at the WHSV of 0.6 h^{-1}, lower than 64 % – 81 % obtained at 1.2 h^{-1}. The catalyst activity consistently improved with IH, regardless of the space velocity value. The oscillations in the ethanol conversion are more evident with CFH than IH, shown in Fig. 3(a) and Fig. 2(a), respectively. These oscillations are independent of reaction temperature but might be related to the low flow rates used in the liquid pump, as shown in Figures S9 and S10.

The rate-determining step (RDS) for non-oxidative ethanol dehydrogenation to acetaldehyde over supported Cu catalysts is the cleavage of the C$_\alpha$-H bond of the surface ethoxide, which is formed by the ethanol adsorption followed by the O-H bond cleavage, as shown in Fig. 4 [33,44]. Alternatively, the RDS of C$_2$-C$_4$ alcohol dehydrogenation can be the O-H bond cleavage when the surface coverage of ethanol is low and shift back to the C$_\alpha$-H bond cleavage when ethanol partial pressure is high [45]. Since the ethanol flow rate is 5 μL/min, such a low flow rate
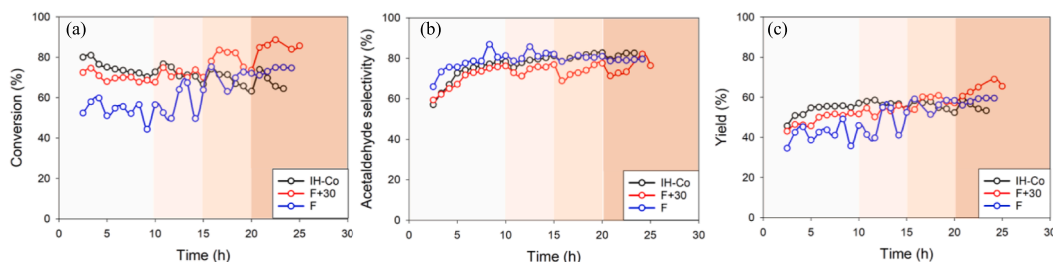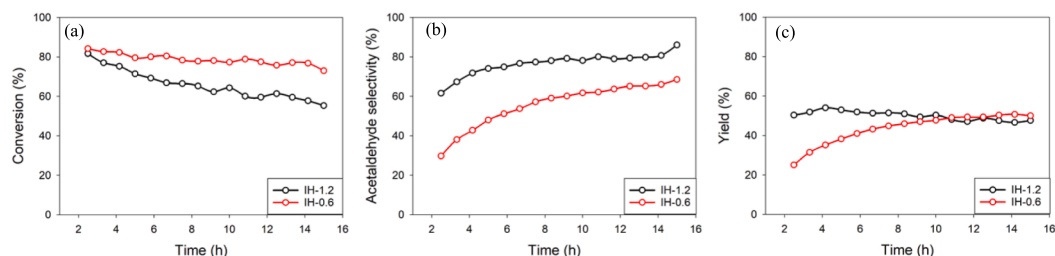

Fig. 1. The (a) conversion of ethanol, (b) selectivity to acetaldehyde, and (c) acetaldehyde yield of ethanol dehydrogenation reaction using 0.2 g Cu/Al$_2$O$_3$ catalyst with IH and furnace heating (F) at 215 ℃ (0 – 10 h), 225 ℃ (10 – 15 h), 235 ℃ (15 – 20 h), and 245 ℃ (20 – 25 h) under atmospheric pressure. The WHSV of ethanol is 1.2 h^{-1}. F+30 denotes the reaction temperature was increased by 30 ℃ to 245 ℃ (0 – 10 h), 255 ℃ (10 – 15 h), 265 ℃ (15 – 20 h), and 275 ℃ (20 – 25 h). The catalyst in the IH system was mixed with Co powder, denoted by IH-Co.
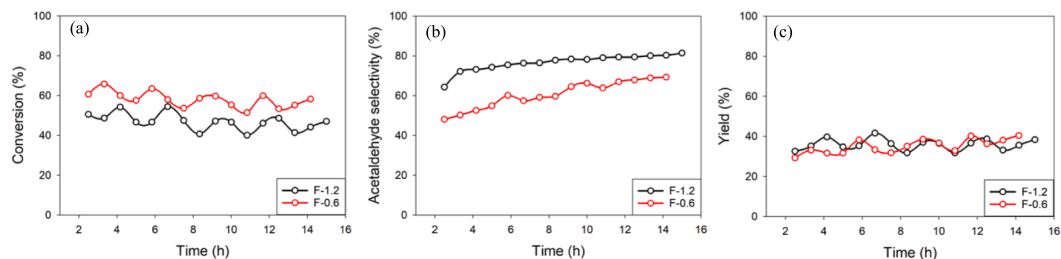
Fig. 2. The (a) conversion of ethanol, (b) selectivity to acetaldehyde, and (c) acetaldehyde yield of ethanol dehydrogenation reaction using 0.2 g Cu/Al$_2$O$_3$ catalyst with IH at 215 ℃ under atmospheric pressure at ethanol WHSV of 0.6 h^{-1} and 1.2 h^{-1}.

Fig. 3. The (a) conversion of ethanol, (b) selectivity to acetaldehyde, and (c) acetaldehyde yield of ethanol dehydrogenation reaction using 0.2 g Cu/Al$_2$O$_3$ catalyst with the CFH at 215 ℃ under atmospheric pressure at ethanol WHSV of 0.6 h^{-1} and 1.2 h^{-1}.
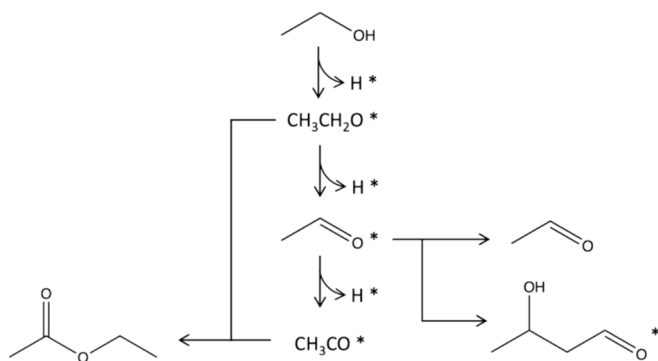

Fig. 4. The ethanol dehydrogenation mechanism. * denotes adsorbed species.

could take longer to reach the steady state and lead to the initial ethanol concentration below 5 % in N$_2$. Therefore, the conversion of ethanol with IH might be facilitated through the facile O-H and C$_\alpha$-H bond cleavage in the magnetic field [46,47]. As shown in Fig. S7 (a) and Fig. S8 (a), the selectivity of ethyl acetate was higher at the beginning and gradually reached a steady state with both heating methods due to the low WHSV of ethanol before reaching the steady state. The initial longer contact time between the ethanol feed and the catalyst active sites leads to more surface ethoxy groups and acetaldehyde formations. Surface acetaldehyde can undergo a successive dehydrogenation step to form surface acetyl, which reacts with the surface ethoxy species to form ethyl acetate. As a result, when the ethanol inlet concentration approached a steady state, the conversion of ethanol and the selectivity to ethyl acetate gradually decreased in the reaction with both heating methods. As shown in Fig. S7 (b) and Fig. S8 (b), the acetone selectivity with IH was high initially and gradually decreased with time while remaining higher than that with CFH. This could be related to the higher ethanol conversion with IH, which resulted in a large amount of surface acetaldehyde species from dissociative ethanol adsorption, providing strongly adsorbed acetaldehyde on the adjacent catalyst active sites that formed adsorbed acetaldol through condensation, leading to acetone formation. In addition, the decrease in acetone production was due to

less surface acetaldehyde formation from the decreasing ethanol conversion with IH. The same trend was observed by Rodrigues *et al.*, where less acetone was formed due to the decrease of acetaldehyde, which is a critical intermediate for acetone production [48].

The Arrhenius plots of acetaldehyde formation calculated far from the equilibrium are shown in Fig. 5. The calculation of Thiele modulus suggested the reaction is not mass-transfer limited (Section S2). The apparent activation energies of ethanol dehydrogenation reaction with CFH and IH are comparable, measuring 19.77 kJ/mol and 24.1 kJ/mol, respectively, consistent with the reported value for high Cu loading catalysts (Table S1[32,42,49–53]). Despite the difference in activation energy, the ethanol conversion with IH is significantly higher than CFH, while the selectivity to acetaldehyde is similar. This suggests that the active sites involved in the reaction are identical with both heating methods. Although there are some works reporting the presence of the magnetic field facilitating the facile bond cleavage and stronger adsorption of intermediates [45–47,54], it is unlikely the reason for the enhanced catalyst activity as the apparent activation energies from IH and CFH are similar. Therefore, the improvement in ethanol conversion with IH can be attributed to the improved local heat transfer between the catalyst particles and Co powder inside the catalyst bed.

3.2. Catalyst bed design

To investigate the heat distribution within the catalyst bed using IH and further improve the catalyst performance, we studied the temperature profile inside the Co heating layers and the catalyst bed in the reactor with COMSOL Multiphysics. As shown in Fig. 6(a), the model simulated the experimental reactor packing with the first configuration, which consisted of four 50 mg Co heating layers separated by quartz wool to heat the incoming ethanol vapor. The catalyst bed has 200 mg Cu/Al$_2$O$_3$ catalyst and 100 mg Co powder. However, the temperature in the Co heating layers in sections A − D is around 447 − 517 ℃, which leads to temperature fluctuations along the reactor length in the z-axis. The increased heat dissipation observed in the Co heating layers suggests an excess supply of energy, resulting in energy wastage. The temperature gradient of 12.5 ℃ across the length of the reactor within the catalyst bed can contribute to suboptimal catalytic performance, including accelerated deactivation and low conversion rates. To
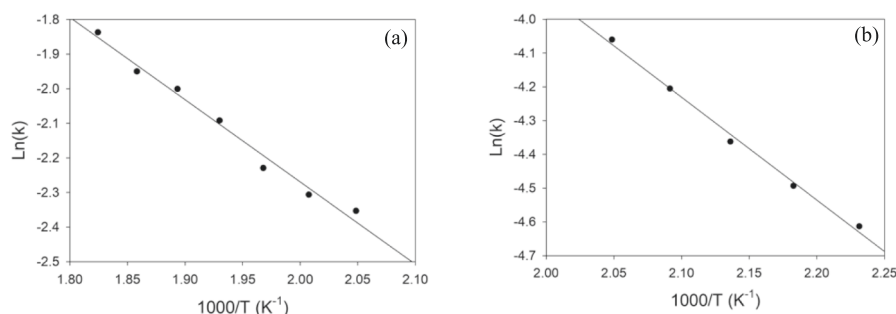
Fig. 5. The Arrhenius plots of acetaldehyde formation rate with (a) furnace heating and (b) IH from ethanol dehydrogenation reaction. The formation rate k is $mol_{acetaldehyde}$/g/h.
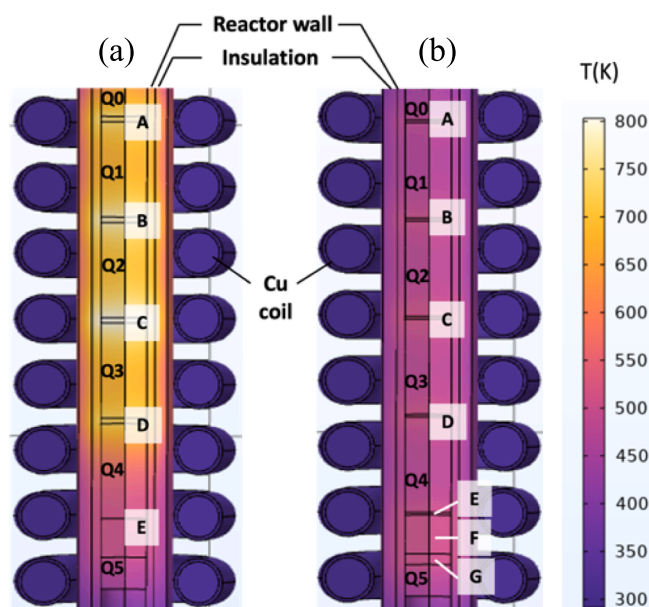

Fig. 6. The temperature distribution inside the reactor with different Co layer configurations. (a) The first design has the same geometry as the experimental setup. 200 mg Cu/Al$_2$O$_3$ catalyst and 100 mg Co mixture is placed in Section E. Detailed dimensions are demonstrated in Fig. S3. (b) The modified configuration with four Co heating layers (Sections A − D) of 20 mg each. Additional Co heating layers of 20 mg (Section E) and 100 mg (Section G) were added above and below the catalyst bed (Section F), respectively. Q0 and Q5 are the quartz wool sections of 5 mm height. Q1 − 4 are the quartz wool sections of 15 mm height to support the Co heating layers.

evaluate the impact of the reaction heat (Qrxn) on the temperature distribution in the catalyst bed, we investigated two extreme cases with the reaction: no acetaldehyde production (selectivity = 0 %) and maximum acetaldehyde production, i.e., equilibrium (selectivity = 80 %). As shown in Fig. S11, the highest increase of 5 ℃ in the catalyst bed temperature was observed when there was no endothermic reaction, suggesting the temperature gradient inside the catalyst bed was mainly caused by the suboptimal bed configuration. Consequently, a new bed design was modeled to lower the temperature of the heating layers and ensure a more uniform temperature distribution within the catalyst bed. As shown in Fig. 6(b), the temperature of the Co heating layers was decreased by 53 % when the amount was reduced to 20 mg in each layer. 20 mg and 100 mg Co layers were added above and below the catalyst bed, respectively, to eliminate the temperature gradient. With the new configuration, the temperature gradient was reduced to 1.5 ℃, the power consumption was significantly lowered by 67 %, and the amount of Co in the reactor remained the same as in the first configuration.

The effectiveness of the new simulated configuration was subsequently validated through experimentation. Fig. 7 illustrates a notable improvement in ethanol conversion and a slower deactivation rate with the new design. Specifically, the ethanol conversion rate with the new design surpasses 1.2 times while maintaining comparable selectivities for acetaldehyde, acetone, and ethyl acetate. As shown in Fig. S12, although the first catalyst bed configuration in IH can reduce the reaction temperature by 30 ℃ compared to CFH at the beginning of the reaction, the deactivation led to a decreased ethanol conversion with time. However, the catalyst activity with the new IH configuration at 215 ℃ was significantly improved and stabilized at the same level as the experiment conducted with CFH at 245 ℃. By the 23-hour mark (t = 23 h), the ethanol conversion reached 69.8 % with the new design, compared to 54.4 % with the first configuration. Therefore, the model can be utilized to optimize the temperature distribution within the reactor, thereby enhancing production and energy efficiency.

With the implementation of the new configuration, the catalyst deactivation during the reaction was mitigated by 38 %. For Cu/Al$_2$O$_3$ catalysts, coking and sintering are reported to be the primary causes of the deactivation in alcohol dehydrogenation reactions [55]. However, from our TGA results (Fig. S13), there was no significant evidence of coke formation on the spent catalysts with both CFH and IH, suggesting coking is not the reason for the deactivation under the reaction conditions reported in this work. Fig. 8 displays the XRD patterns of the spent, reduced, and fresh catalysts within the 2θ range of 20° − 90°. The Cu (1 1 1) reflex at 2θ = 43.3° is used to estimate the Cu crystallite sizes by the Debye-Scherrer equation. As shown in Fig. 8, the Cu crystallite sizes of the freshly reduced samples with IH and CFH are 20.5 nm and 20.6 nm, respectively, suggesting the initial crystallite size of the reduced Cu/Al$_2$O$_3$ catalyst was not affected by the different heating methods. The crystallite sizes corresponding to the spent catalysts after the reaction at 215 ℃ with the old configuration with IH, 215 ℃ with the new design with IH, 215 ℃ with CFH, and 245 ℃ with CFH are 25 nm, 20.8 nm, 21.8 nm, and 23.8 nm, respectively. Previous studies have shown that the average crystallite size growth exceeding 2 nm can lead to the sintering of the supported Cu catalysts [56]. In our study, both spent catalysts after reaction at 215 ℃ and 245 ℃ with CFH for 15 h did not show apparent deactivation, even with a 3.2 nm increase in the Cu crystallite size. The largest crystallite size was observed on the sample with IH prior to modifying the catalyst bed configuration, showing that sintering might lead to accelerated deactivation under this reaction condition. The spent sample with IH with the new bed configuration, however, showed a significantly reduced crystallite size compared with the old configuration, suggesting the sintering was alleviated after the bed optimization with modeling. As a result, the catalyst activity from the new design can presumably be further improved with the modeling. Cu^{1+} and Cu^{2+} peaks from the spent IH samples, as well as Cu (2 2 0) and Co fcc peaks at 2θ = 73.4° and 76° from the spent IH sample with the new configuration, were not observed in the stacked XRD patterns in Fig. 8 but were shown in the raw data (Fig. S14). This is attributed to the B-
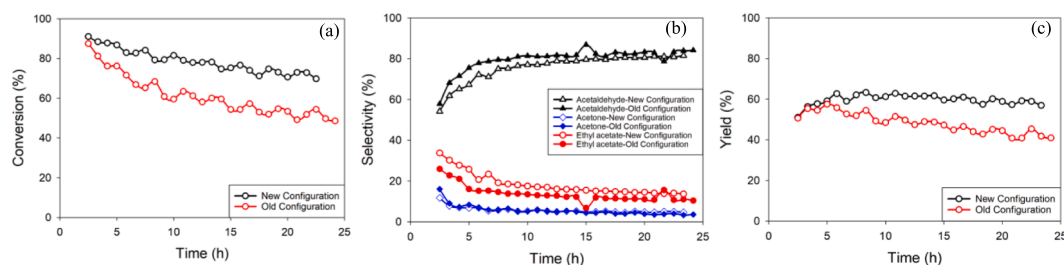
Fig. 7. The comparison of (a) the ethanol conversion, (b) the selectivities of acetaldehyde, acetone, and ethyl acetate, and (c) the yield of acetaldehyde between the new and the old configurations.
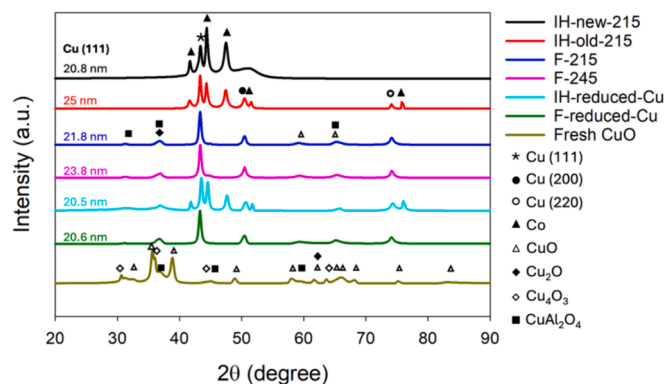

Fig. 8. The XRD patterns of the spent catalysts with the new bed configuration with IH at 215 ℃ (IH-new-215), the old bed configuration with IH at 215 ℃ (IH-old-215), with CFH at 215 ℃ (F-215), with CFH at 245 ℃ (F-245). The catalysts are reduced with IH (IH-reduced-Cu) and CFH (F-reduced-Cu). The Cu (1 1 1) sizes were labeled above each sample plot.

spline smoothing applied to the raw data (Fig. S14) with a high noise-to-intensity ratio due to the complex mixture of the quartz wool and a large amount of Co powder. Additional susceptor Co hcp and fcc peaks were shown at $2\theta = 41.6°, 44.3°$ in the samples with IH.

4. Conclusions

Our study demonstrates that IH can improve production efficiency by lowering the reaction temperature by 30 ℃ in the ethanol dehydrogenation to acetaldehyde reaction thanks to the minimal temperature gradient within the catalyst bed, enhanced local heat transfer, and the rapid compensation for temperature changes facilitated by the close contact between the susceptor materials and the catalyst. IH achieved lower energy consumption due to its instantaneous and targeted heating, which overcomes heat transfer limitations compared to CFH.

We developed a transport model to investigate the temperature profile within the catalyst bed, which is a critical factor affecting the catalyst activity with IH. Furthermore, a new catalyst bed configuration was designed and confirmed through experimentation, demonstrating that catalyst performance can be further improved by minimizing the temperature gradient. Due to the intrinsic limitation of the laser pyrometer, which only measures the surface temperature of the catalyst bed, the temperature distribution inside the catalyst bed can only be predicted through the heat transfer model. Although one can measure similar reaction temperatures through the quartz reactor wall, the heat distribution inside the catalyst bed can be largely affected by the packing without a proper bed configuration design, leading to decreased catalyst performance. As a result, a heat transfer model is necessary to optimize the bed configuration, decrease the temperature gradient in the catalyst bed, and improve the catalyst stability. The power consumption of the reactor was reduced by 67 % with the new design, and the catalyst

deactivation was slowed down with the new configuration, such that both high production and energy efficiency can be achieved by applying IH. These results serve as proof of concept, demonstrating the feasibility of using IH in catalyst beds for the dehydrogenation of ETAA. ETAA is the first step of the Ostromislensky process for 1,3-butadiene production from ethanol, where acetaldehyde is an intermediate for the second step reaction. With the possibility of the two-step Ostromislensky process with IH, we can potentially have better control over product selectivities compared to the industrially available Lebedev process and scale it up for industrial applications. These findings open opportunities for further exploration and investigation using ethanol as a raw material and induction heated catalyst beds [57].

CRediT authorship contribution statement

Han Wang: Writing – original draft, Methodology, Formal analysis, Data curation. **Ben Ko:** Validation, Software, Investigation, Formal analysis, Data curation. **John O'Donnell-Sloan:** Software, Investigation, Formal analysis. **John Minh Quang Pham:** Investigation, Data curation. **Hannah Schutte:** Investigation. **Nicholas Wang:** Investigation. **Carlos Lizandara-Pueyo:** Writing – review & editing, Project administration. **Jian-Ping Chen:** Writing – review & editing, Supervision. **Erdem Sasmaz:** Writing – review & editing, Supervision, Resources, Project administration, Funding acquisition, Conceptualization.

Declaration of competing interest

The authors declare that they have no known competing financial interests or personal relationships that could have appeared to influence the work reported in this paper.

Data availability

Data will be made available on request.

Acknowledgments

Appendix A. Supplementary data

Supplementary data to this article can be found online at https://doi.org/10.1016/j.cej.2024.154187.

References

[1] D.S. Mallapragada, Y. Dvorkin, M.A. Modestino, D.V. Esposito, W.A. Smith, B. M. Hodge, M.P. Harold, V.M. Donnelly, A. Nuz, C. Bloomquist, K. Baker, L. C. Grabow, Y. Yan, N.N. Rajput, R.L. Hartman, E.J. Biddinger, E.S. Aydil, A. D. Taylor, Decarbonization of the chemical industry through electrification: Barriers and opportunities, Joule. 7 (2023) 23–41, https://doi.org/10.1016/j. joule.2022.12.008.

[2] J.A. Chavez Velasco, M. Tawarmalani, R. Agrawal, Systematic Analysis Reveals Thermal Separations Are Not Necessarily Most Energy Intensive, Joule. 5 (2021) 330–343, https://doi.org/10.1016/j.joule.2020.12.002.

[3] I. Julian, C.M. Pedersen, A.B. Jensen, A.K. Baden, J.L. Hueso, A.V. Friderichsen, H. Birkedal, R. Mallada, J. Santamaria, From bench scale to pilot plant: A 150x scaled-up configuration of a microwave-driven structured reactor for methane dehydroaromatization, Catal. Today. 383 (2022) 21–30, https://doi.org/10.1016/ j.cattod.2021.04.013.

[4] A. Meffre, B. Mehdaoui, V. Connord, J. Carrey, P.F. Fazzini, S. Lachaize, M. Respaud, B. Chaudret, Complex nano-objects displaying both magnetic and catalytic properties: A proof of concept for magnetically induced heterogeneous catalysis, Nano Lett. 15 (2015) 3241–3248, https://doi.org/10.1021/acs. nanolett.5b00446.

[5] Y.T. Kim, J.J. Lee, J. Lee, Electricity-driven reactors that promote thermochemical catalytic reactions via joule and induction heating, Chem. Eng. J. 470 (2023) 144333, https://doi.org/10.1016/j.cej.2023.144333.

[6] S. Ruta, R. Chantrell, O. Hovorka, Unified model of hyperthermia via hysteresis heating in systems of interacting magnetic nanoparticles, Sci. Rep. 5 (2015) 9090, https://doi.org/10.1038/srep09090.

[7] T.K. Houlding, E.V. Rebrov, Application of alternative energy forms in catalytic reactor engineering, Green Process. Synth. 1 (2012), https://doi.org/10.1515/ greenps-2011-0502.

[8] W. Wang, G. Tuci, C. Duong-Viet, Y. Liu, A. Rossin, L. Luconi, J.-M. Nhut, L. Nguyen-Dinh, C. Pham-Huu, G. Giambastiani, Induction Heating: An Enabling Technology for the Heat Management in Catalytic Processes, ACS Catal. 9 (2019) 7921–7935, https://doi.org/10.1021/acscatal.9b02471.

[9] B. Whajah, N. Da Silva Moura, J. Blanchard, S. Wicker, K. Gandar, J.A. Dorman, K. M. Dooley, Catalytic Depolymerization of Waste Polyolefins by Induction Heating: Selective Alkane/Alkene Production, Ind. Eng. Chem. Res. 60 (2021) 15141–15150, https://doi.org/10.1021/acs.iecr.1c02674.

[10] A. Bordet, L.M. Lacroix, P.F. Fazzini, J. Carrey, K. Soulantica, B. Chaudret, Magnetically Induced Continuous CO2 Hydrogenation Using Composite Iron Carbide Nanoparticles of Exceptionally High Heating Power, Angew. Chemie - Int. Ed. 55 (2016) 15894–15898, https://doi.org/10.1002/anie.201609477.

[11] M.R. Almind, S.B. Vendelbo, M.F. Hansen, M.G. Vinum, C. Frandsen, P. M. Mortensen, J.S. Engbæk, Improving performance of induction-heated steam methane reforming, Catal. Today. 342 (2020) 13–20, https://doi.org/10.1016/J. CATTOD.2019.05.005.

[12] M.G. Vinum, M.R. Almind, J.S. Engbæk, S.B. Vendelbo, M.F. Hansen, C. Frandsen, J. Bendix, P.M. Mortensen, Dual-Function Cobalt-Nickel Nanoparticles Tailored for High-Temperature Induction-Heated Steam Methane Reforming, Angew. Chemie - Int. Ed. 57 (2018) 10569–10573, https://doi.org/10.1002/anie.201804832.

[13] W. Wang, C. Duong-Viet, G. Tuci, Y. Liu, A. Rossin, L. Luconi, J.M. Nhut, L. Nguyen-Dinh, G. Giambastiani, C. Pham-Huu, Highly Nickel-Loaded γ-Alumina Composites for a Radiofrequency-Heated, Low-Temperature CO2 Methanation Scheme, ChemSusChem. 13 (2020) 5468–5479, https://doi.org/10.1002/ cssc.202001885.

[14] N. Chidhambaram, S.J.J. Kay, S. Priyadharshini, R. Meenakshi, P. Sakthivel, S. Dhanbalan, S. Shanavas, S.K. Kamaraj, A. Thirumurugan, Magnetic Nanomaterials as Catalysts for Syngas Production and Conversion, Catalysts. 13 (2023), https://doi.org/10.3390/catal13020440.

[15] W. Donphai, N. Kunthakudee, J. Munpollasri, P. Sangteantong, S. Tonlublao, W. Limphirat, Y. Poo-Arporn, S. Kiatphuengporn, M. Chareonpanich, Application of magnetic field to CO hydrogenation using a confined-space catalyst: effect on reactant gas diffusivity and reactivity, RSC Adv. 11 (2021) 3990–3996, https://doi. org/10.1039/d0ra09870a.

[16] W. Donphai, N. Piriyawate, T. Witoon, P. Jantaratana, V. Varabuntoonvit, M. Chareonpanich, Effect of magnetic field on CO2 conversion over Cu-ZnO/ZrO2 catalyst in hydrogenation reaction, J. CO2 Util. 16 (2016) 204–211, https://doi. org/10.1016/j.jcou.2016.07.007.

[17] Z. Du, R. Chotchaipitakkul, P. Sangteantong, W. Donphai, W. Limphirat, Y. Poo-arporn, S. Nijpanich, S. Kiatphuengporn, P. Jantaratana, M. Chareonpanich, Catalytic LPG Conversion Over Fe-Ga Modified ZSM-5 Zeolite Catalysts with Different Particle Sizes: Effect of Confined-Space Zeolite and External Magnetic Field, Top. Catal. 66 (2023) 1594–1607, https://doi.org/10.1007/s11244-023-01825-4.

[18] D. Kim, I. Efe, H. Torlakcik, A. Terzopoulou, A. Veciana, E. Siringil, F. Mushtaq, C. Franco, D. von Arx, S. Sevim, J. Puigmartí-Luis, B. Nelson, N.A. Spaldin, C. Gattinoni, X.Z. Chen, S. Pané, Magnetoelectric Effect in Hydrogen Harvesting: Magnetic Field as a Trigger of Catalytic Reactions, Adv. Mater. 34 (2022), https:// doi.org/10.1002/adma.202110612.

[19] Y. Li, B. Zhao, H. Guan, S. Liu, D. Zhu, A. Song, H. Li, L. Sun, Hydrogen Production from Catalytic Pyrolysis of Phenol as Tar Model Compound in Magnetic Field, Energies. 16 (2023), https://doi.org/10.3390/en16104140.

[20] H. Pan, X. Jiang, X. Wang, Q. Wang, M. Wang, Y. Shen, Effective Magnetic Field Regulation of the Radical Pair Spin States in Electrocatalytic CO2 Reduction, J. Phys. Chem. Lett. 11 (2020) 48–53, https://doi.org/10.1021/acs. jpclett.9b03146.

[21] K. Roy, P. Devi, P. Kumar, Magnetic-field induced sustainable electrochemical energy harvesting and storage devices: Recent progress, opportunities, and future perspectives, Nano Energy. 87 (2021) 106119, https://doi.org/10.1016/j. nanoen.2021.106119.

[22] S. Zhong, X. Guo, A. Zhou, Z. Chen, D. Jin, M. Fan, T. Ma, Fundamentals and Recent Progress in Magnetic Field Assisted CO2 Capture and Conversion, Small. 20 (2024) 1–21, https://doi.org/10.1002/smll.202305533.

[23] J. Marbaix, N. Mille, L.M. Lacroix, J.M. Asensio, P.F. Fazzini, K. Soulantica, J. Carrey, B. Chaudret, Tuning the Composition of FeCo Nanoparticle Heating Agents for Magnetically Induced Catalysis, ACS Appl. Nano Mater. 3 (2020) 3767–3778, https://doi.org/10.1021/acsanm.0c00444.

[24] S. Ceylan, C. Friese, C. Lammel, K. Mazac, A. Kirschning, Inductive heating for organic synthesis by using functionalized magnetic nanoparticles inside microreactors, Angew. Chemie - Int. Ed. 47 (2008) 8950–8953, https://doi.org/ 10.1002/anie.200801474.

[25] S.S. Kale, J.M. Asensio, M. Estrader, M. Werner, A. Bordet, D. Yi, J. Marbaix, P. F. Fazzini, K. Soulantica, B. Chaudret, Iron carbide or iron carbide/cobalt nanoparticles for magnetically-induced CO2 hydrogenation over Ni/SiRAlOx catalysts, Catal. Sci. Technol. 9 (2019) 2601–2607, https://doi.org/10.1039/ c9cy00437h.

[26] S. Velasco, F.L. Román, Determining the Curie Temperature of Iron and Nickel, Phys. Teach. 45 (2007) 387–389, https://doi.org/10.1119/1.2768702.

[27] S. Liu, Y. Wang, T. McDonald, S.E. Taylor, Efficient production of biodiesel using radio frequency heating, Energy and Fuels. 22 (2008) 2116–2120, https://doi.org/ 10.1021/ef800038g.

[28] D. Lupu, A.R. Biriş, A. Jianu, C. Bunescu, E. Burkel, E. Indrea, G. Mihăilescu, S. Pruneanu, L. Olenic, I. Mişan, Carbon nanostructures produced by CCVD with induction heating, Carbon n. y. 42 (2004) 503–507, https://doi.org/10.1016/j. carbon.2003.12.034.

[29] A.R. Biris, A.S. Biris, D. Lupu, S. Trigwell, E. Dervishi, Z. Rahman, P. Marginean, Catalyst excitation by radio frequency for improved carbon nanotubes synthesis, Chem. Phys. Lett. 429 (2006) 204–208, https://doi.org/10.1016/j. cplett.2006.08.007.

[30] P.M. Mortensen, J.S. Engbæk, S.B. Vendelbo, M.F. Hansen, M. Østberg, Direct Hysteresis Heating of Catalytically Active Ni-Co Nanoparticles as Steam Reforming Catalyst, Ind. Eng. Chem. Res. 56 (2017) 14006–14013, https://doi.org/10.1021/ acs.iecr.7b02331.

[31] J. Pang, M. Zheng, C. Wang, X. Yang, H. Liu, X. Liu, J. Sun, Y. Wang, T. Zhang, Hierarchical Echinus-like Cu-MFI Catalysts for Ethanol Dehydrogenation, ACS Catal. 10 (2020) 13624–13629, https://doi.org/10.1021/acscatal.0c03860.

[32] Q.N. Wang, L. Shi, A.H. Lu, Highly Selective Copper Catalyst Supported on Mesoporous Carbon for the Dehydrogenation of Ethanol to Acetaldehyde, ChemCatChem. 7 (2015) 2846–2852, https://doi.org/10.1002/cctc.201500501.

[33] Z.T. Wang, Y. Xu, M. El-Soda, F.R. Lucci, R.J. Madix, C.M. Friend, E.C.H. Sykes, Surface Structure Dependence of the Dry Dehydrogenation of Alcohols on Cu(111) and Cu(110), J. Phys. Chem. c. 121 (2017) 12800–12806, https://doi.org/ 10.1021/acs.jpcc.7b02957.

[34] C. Angelici, B.M. Weckhuysen, P.C.A. Bruijnincx, Chemocatalytic conversion of ethanol into butadiene and other bulk chemicals, ChemSusChem. 6 (2013) 1595–1614, https://doi.org/10.1002/cssc.201300214.

[35] J. Shan, N. Janvelyan, H. Li, J. Liu, T.M. Egle, J. Ye, M.M. Biener, J. Biener, C. M. Friend, R.J. Madix, M. Flytzani-Stephanopoulos, Selective non-oxidative dehydrogenation of ethanol to acetaldehyde and hydrogen on highly dilute NiCu alloys, Appl. Catal. B Environ. 205 (2017) 541–550, https://doi.org/10.1016/j.apcatb.2016.12.045.

[36] M.R. Almind, M.G. Vinum, S.T. Wismann, M.F. Hansen, S.B. Vendelbo, J. S. Engbæk, P.M. Mortensen, I. Chorkendorff, C. Frandsen, Optimized CoNi Nanoparticle Composition for Curie-Temperature-Controlled Induction-Heated Catalysis, ACS Appl. Nano Mater. 4 (2021) 11537–11544, https://doi.org/ 10.1021/acsanm.1c01941.

[37] J. Chen, A. Kundu, M. Angel. Copper Extrudate Catalyst and Applications for Hydrogenation and Hydrogenolysis , 2022. https://lens.org/102-917-621-998-233.

[38] A. Akbari, E. Mohammadian, S.A. Alavi Fazel, M. Shanbedi, M. Bahreini, M. Heidari, P. Babakhani Dehkordi, S.N. Che Mohamed Hussein, Natural Convection from the Outside Surface of an Inclined Cylinder in Pure Liquids at Low Flux, ACS Omega. 4 (2019) 7038–7046. https://doi.org/10.1021/acsomega.9b00176.

[39] C. Khe, A. Azizan, Z. Lockman, Formation of Truncated Hexagonal Bipyramid Cobalt Superstructures via a Formation of Truncated Hexagonal Bipyramid Cobalt Superstructures via a Polyol Route and Its Magnetic Properties, J. Mater. Sci. Eng. 5 (2011) 378–385.

[40] P. Liu, E.J.M. Hensen, Highly efficient and robust Au/MgCuCr2O4 catalyst for gas-phase oxidation of ethanol to acetaldehyde, J. Am. Chem. Soc. 135 (2013) 14032–14035, https://doi.org/10.1021/ja406820f.

[41] C.L. Roman, N. Da Silva Moura, S. Wicker, K.M. Dooley, J.A. Dorman, Induction Heating of Magnetically Susceptible Nanoparticles for Enhanced Hydrogenation of Oleic Acid, ACS Appl. Nano Mater. 5 (2022) 3676–3685, https://doi.org/10.1021/ acsanm.1c04351.

[42] M.Y. Li, W.D. Lu, L. He, F. Schüth, A.H. Lu, Tailoring the Surface Structure of Silicon Carbide Support for Copper Catalyzed Ethanol Dehydrogenation, ChemCatChem. 11 (2019) 481–487, https://doi.org/10.1002/cctc.201801742.

[43] K. Inui, T. Kurabayashi, S. Sato, Direct synthesis of ethyl acetate from ethanol carried out under pressure, J. Catal. 212 (2002) 207–215, https://doi.org/ 10.1006/jcat.2002.3769.

[44] M. Bowker, R.J. Madix, XPS, UPS and thermal desorption studies of alcohol adsorption on Cu(110). I. Methanol, Surf. Sci. 95 (1980) 190–206. https://doi.org/ 10.1016/0039-6028(80)90135-1.

[45] S. Hanukovich, A. Dang, P. Christopher, Influence of Metal Oxide Support Acid Sites on Cu-Catalyzed Nonoxidative Dehydrogenation of Ethanol to Acetaldehyde, ACS Catal. 9 (2019) 3537–3550, https://doi.org/10.1021/acscatal.8b05075.

[46] Q. Huang, S. Xie, J. Hao, Z. Ding, C. Zhang, H. Sheng, J. Zhao, Spin-Enhanced O−H Cleavage in Electrochemical Water Oxidation, Angew. Chemie - Int. Ed. 62 (2023) 1–6, https://doi.org/10.1002/anie.202300469.

[47] W. Jia, Z. Fan, A. Du, L. Shi, Untargeted foodomics reveals molecular mechanism of magnetic field effect on Feng-flavor Baijiu ageing, Food Res. Int. 149 (2021), https://doi.org/10.1016/j.foodres.2021.110681.

[48] C.P. Rodrigues, P.C. Zonetti, C.G. Silva, A.B. Gaspar, L.G. Appel, Chemicals from ethanol - The acetone one-pot synthesis, Appl. Catal. A Gen. 458 (2013) 111–118, https://doi.org/10.1016/j.apcata.2013.03.028.

[49] A.G. Sato, D.P. Volanti, I.C. De Freitas, E. Longo, J.M.C. Bueno, Site-selective ethanol conversion over supported copper catalysts, Catal. Commun. 26 (2012) 122–126, https://doi.org/10.1016/j.catcom.2012.05.008.

[50] H. Zhang, H.R. Tan, S. Jaenicke, G.K. Chuah, Highly efficient and robust Cu catalyst for non-oxidative dehydrogenation of ethanol to acetaldehyde and hydrogen, J. Catal. 389 (2020) 19–28, https://doi.org/10.1016/j.jcat.2020.05.018.

[51] S.Q. Cheng, X.F. Weng, Q.N. Wang, B.C. Zhou, W.C. Li, M.R. Li, L. He, D.Q. Wang, A.H. Lu, Defect-rich BN-supported Cu with superior dispersion for ethanol conversion to aldehyde and hydrogen, Chinese, J. Catal. 43 (2022) 1092–1100, https://doi.org/10.1016/S1872-2067(21)63891-3.

[52] J. Shan, J. Liu, M. Li, S. Lustig, S. Lee, M. Flytzani-Stephanopoulos, NiCu single atom alloys catalyze the C-H bond activation in the selective non- oxidative ethanol dehydrogenation reaction, Appl. Catal. B Environ. 226 (2018) 534–543, https://doi.org/10.1016/j.apcatb.2017.12.059.

[53] G. Pampararo, G. Garbarino, P. Riani, M. Villa García, V. Sánchez Escribano, G. Busca, A study of ethanol dehydrogenation to acetaldehyde over supported copper catalysts: Catalytic activity, deactivation and regeneration, Appl. Catal. A Gen. 602 (2020) 117710, https://doi.org/10.1016/j.apcata.2020.117710.

[54] H.M. Nguyen, C.M. Phan, S. Liu, C. Pham-Huu, L. Nguyen-Dinh, Radio-frequency induction heating powered low-temperature catalytic CO_2 conversion via bi-reforming of methane, Chem. Eng. J. 430 (2022) 132934, https://doi.org/10.1016/j.cej.2021.132934.

[55] D. Yu, W. Dai, G. Wu, N. Guan, L. Li, Stabilizing copper species using zeolite for ethanol catalytic dehydrogenation to acetaldehyde, Chinese, J. Catal. 40 (2019) 1375–1384, https://doi.org/10.1016/S1872-2067(19)63378-4.

[56] Y. Xing, Z. Liu, S.L. Suib, Inorganic synthesis for the stabilization of nanoparticles: Application to Cu/Al2O3 nanocomposite materials, Chem. Mater. 19 (2007) 4820–4826, https://doi.org/10.1021/cm0712570.

[57] E. Sasmaz, H. Wang, C. Lizandara-Pueyo, J.-P. Chen, A. Gokhale, Tuning Reaction Selectivity with Induction Heating, Provisional Patent Application US63/536555 (2023).